J. Fluid Mech. (2024), *vol*. 1000, A53, doi:10.1017/jfm.2024.646

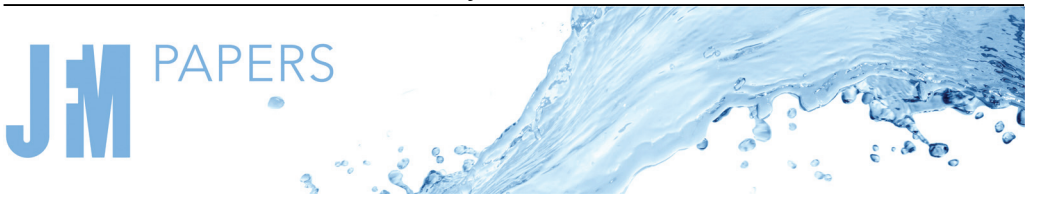

Energetics of mode-1 internal waves interacting with topographic ridges of varying height and slope

Matthew R. Klema[1,2] **and Subhas K. Venayagamoorthy**[2,†]

[1]Physics & Engineering Department, Fort Lewis College, Durango, CO 81301, USA

[2]Department of Civil and Environmental Engineering, Colorado State University, Fort Collins, CO 80523, USA

(Received 10 June 2023; revised 6 March 2024; accepted 8 June 2024)

Energetics of mode-1 internal waves interacting with topographic ridges are investigated using high-resolution two-dimensional simulations at spatial scales of $O(100)$ m that span between classical laboratory-scale ($O(10)$ m) and field-scale simulations ($O(1000–10\,000)$ m). This paper focuses on the energetics of wave–topography interaction, with emphasis on systematically examining the partitioning of the incident wave energy as a function of wave forcing and topographic parameters. Partitioning of energy into the transmitted, reflected and dissipated components is quantified as a function of wave Froude number $Fr = U_0/c_{ph}$ (U_0 = velocity amplitude of forcing and c_{ph} = internal wave celerity), slope criticality = γ/s, where γ = topographic slope and s = wave characteristic slope, and the ratio of topographic height h_t to water depth d. As Fr increases, dense fluid from the base of the stratified water column surges upslope with significant vertical inertia, leading to the formation of internal boluses that plunge over and onto the downstream side of the ridge, resulting in elevated dissipation. Results show that non-hydrostatic contributions to the total energy flux are significant (up to 50 %). Analysis of the energy flux budget shows that transmitted energy flux decreases monotonically as γ/s increases for any given Fr and h_t/d. At critical slopes ($\gamma/s = 1$), the transmitted energy flux scales as a linear function of h_t/d, with a mild dependence on Fr, a key result that can be useful in energy flux parameterizations. Reflected energy flux exhibits a nonlinear dependence on the ridge height, increasing sharply when $h_t/d > 0.5$. Dissipation is enhanced at critical slopes, with a plateau evident for $\gamma/s \geq 1$ and $h_t/d = 0.5$ for all Fr.

Key words: internal waves, stratified flows, topographic effects

† Email address for correspondence: vskaran@colostate.edu

1. Introduction

In oceanography the study of the interactions of internal waves with topography is an area of research that sees continual attention. This is because such interactions are thought to be one of the main sources of energy for sustaining ocean mixing. Thus, understanding the process and flow structures that develop as a result of this interaction remains as important to the understanding of oceanic processes as ever (Baines & Hoinka 1985; Munk & Wunsch 1998). Surface tides and wind create sources of mechanical energy that can convert to internal waves (St. Laurent & Garrett 2002; Wunsch & Ferrari 2004; Garrett & Kunze 2007). Internal waves can be generated from wave–wave interactions (Nikurashin & Legg 2011), lee-wave release resulting from a changing internal tide (Gayen & Sarkar 2011) and from the interaction of first-mode internal tides with topography (Holloway & Merrifield 1999; Klymak *et al.* 2006; Levine & Boyd 2006). Despite having observations and measurement of these features, questions remain about the development, evolution and fate of internal waves due to the complex dynamics of their interaction with topography which can be difficult to measure directly in the field (Vlasenko & Hutter 2002). Furthering our understanding of the nonlinear internal wave dynamics has implications for our understanding of the processes that drive energy transport and mixing in the oceans.

Breaking nonlinear internal waves occur when topography is encountered that has a slope that matches the internal wave group velocity as described by Phillips (1977). Field measurements have confirmed that significant amounts of turbulent mixing occur as a result of the internal wave field interacting with oceanic ridges, seamounts, continental slopes and underwater channels (Munk & Wunsch 1998; Kunze & Smith 2004; Polzin 2009; Alford *et al.* 2011; Ledwell *et al.* 2011; Buijsman, Legg & Klymak 2012; Pinkel, Buijsman & Klymak 2012; Alford, Klymak & Carter 2014; Cusack *et al.* 2019; Girton *et al.* 2019; Srinivasan *et al.* 2019; Zheng & Nikurashin 2019). The dynamics resulting from these interactions converts energy from the internal wave field and may be a main source available for vertical mixing of the water column. This mixing results in flow gradients that drive global oceanic circulation. Understanding these processes has been bolstered by an increasing knowledge of baroclinic tide generation and turbulence (Llewellyn Smith & Young 2002; Althaus, Kunze & Sanford 2003; Llewellyn Smith & Young 2003; Nash *et al.* 2004; Carter, Gregg & Lien 2005; Garrett & Kunze 2007; Gayen & Sarkar 2010; Musgrave *et al.* 2016, 2017; Sarkar & Scotti 2017; Shakespeare & Hogg 2019) where low first-mode internal waves allow for propagation of energy far from these sources (Ray & Mitchum 1996; Alford *et al.* 2007) as well theoretical modelling (Bell 1975; Balmforth, Ierley & Young 2002; Llewellyn Smith & Young 2002; Khatiwala 2003; Laurent *et al.* 2003; Aguilar, Sutherland & Muraki 2006). In addition to field observations, numerous laboratory studies have been performed to study the interaction of internal waves with topography (Cacchione & Wunsch 1974; Ivey & Nokes 1989; Ivey, Winters & De Silva 2000; Troy & Koseff 2005; Hult, Troy & Koseff 2006; Moore, Koseff & Hult 2016).

Computational fluid dynamics (CFD) has become one of the most important tools aiding the study and understanding of stratified flow processes. As a result, studies using CFD to study the internal wave–topography interactions are increasingly prevalent. Work in this area has largely fallen into two broad categories; direct numerical simulations (DNS) that resolve the turbulent processes near the laboratory scale ($O \leq 10$ m) (i.e. Slinn & Riley 1998; Javam, Imberger & Armfield 1999; Venayagamoorthy & Fringer 2006; Rapaka, Gayen & Sarkar 2013; Jalali, Rapaka & Sarkar 2014; Lamb 2014; Lamb & Dunphy 2018; Puthan, Pawlak & Sarkar 2022) and relatively larger field-scale simulations ($O \geq 1000$ m) that do not resolve the full flow structure (i.e. Aguilar & Sutherland 2006;

Legg & Klymak 2008; Klymak *et al.* 2012; Winters & Armi 2013; Legg 2014; Gemmrich & Klymak 2015; Srinivasan *et al.* 2019; Perfect, Kumar & Riley 2020*a*,*b*). Within the study of this problem there is a body of work using field-scale simulation to address the breaking and scattering of internal waves interacting with a highly supercritical topography (e.g. Laurent *et al.* (2003), Klymak *et al.* (2006), Klymak, Legg & Pinkel (2010), Klymak *et al.* (2012) and references therein). In particular, the works of Laurent *et al.* (2003) and Klymak *et al.* (2013) discuss the internal tidal generation, scattering and dissipation associated with surface tides interacting with a highly supercritical and abrupt topography using theoretical and numerical simulations.

More recently there has been an increasing number of studies that use large eddy simulation (LES) in order to simulate more realistic flow structures near topography (Armenio & Sarkar 2002; Jalali & Sarkar 2017; Puthan *et al.* 2020; Puthan, Sarkar & Pawlak 2021). Venayagamoorthy & Fringer (2006) considered the generation of upslope propagating bores leading directly to dissipation and mixing for a variety of mode-1 internal wave forcings and slope steepnesses at a shelf break. Legg & Adcroft (2003) completed Reynolds-averaged Navier–Stokes (RANS) simulations of field-scale topography with slopes of various monotonic shapes. Studies using numerical modelling of this interaction have been completed for subcritical and critical slope cases (Legg & Klymak 2008; Legg 2014) as well as for critical and supercritical cases (Klymak *et al.* 2012; Hall, Huthnance & Williams 2013). Works at the laboratory scale by Rapaka *et al.* (2013), Chalamalla & Sarkar (2015) and Puthan *et al.* (2022) have emphasized the importance of the energetics and turbulence from DNS of ridges or seamounts at the laboratory scale. There are a wide range of codes that have been developed for simulation of geophysical flows; see the references above for each specific code. Despite the large body of work on this topic, there remains much to be understood regarding the energetics and nonlinear dynamics of interaction processes with a particular emphasis on the energy partitioning, dissipation and mixing.

The goal of this study is to systematically explore the energetics and ensuing mixing from the interaction of low-mode internal waves with a ridge, which is a common archetypal topographic feature found in the ocean. In particular, the key questions to be investigated are: What is the partitioning of the incident internal wave energy over the course of the interaction with a topographic ridge? Under what topographic and wave forcing conditions do incoming low-mode waves break and lead to the formation of nonlinear bores? And how much dissipation and mixing occurs in the vicinity of the ridge? These questions are very important in many respects and their answers have important implications for the conclusions drawn from both numerical models and field observations focusing on breaking internal waves interacting with topographic features. These questions are investigated using high-resolution two-dimensional numerical simulations of the interaction of a first-mode internal wave field with a topographic ridge meant to emulate oceanic ridges found around the globe and which are recognized hotspots for turbulent mixing (Munk & Wunsch 1998). Analysis closely follows the structure presented in Venayagamoorthy & Fringer (2006) (hereafter VF06). However, the emphasis here is on investigating the partitioning and flux of energy from internal wave interaction with different topographic ridges (i.e. varying height and slope steepness) as opposed to a shelf as was investigated by VF06. The choice of a topographic ridge is similar to Rapaka *et al.* (2013) but simulations in our analysis are completed at a relatively larger scale, $O(100\ \mathrm{m})$. Legg & Klymak (2008) and Legg (2014) (hereafter L14) also show CFD results of internal wave interaction with a ridge but at the full field scale, $O(10^3–10^6\ \mathrm{m})$, which results do not resolve flow structures.

This simulation study aims to provide a needed bridge to tie results between the highly resolved DNS at the laboratory scale, exemplified by VF06 and Rapaka *et al.* (2013), and the RANS simulations generally used for modelling of internal waves at the field scale, exemplified by L14. Additionally, the analysis aims to show that, through careful parameter choice and modelling consideration, not all turbulent flow structures need to be resolved to achieve comparable results to DNS in terms of both the qualitative flow structures and quantitative calculations of important flow quantities such as energy flux. The numerical methods, formulation and simulation set-up are discussed in § 2. The results and discussion of the wave–topography interaction are given in § 3, with conclusions given in § 4.

2. Formulation and numerical methods

Equation (2.1) is the Navier–Stokes equation with the Boussinesq approximation and a constant kinematic viscosity ν, which is subjected to the continuity constraint given by (2.2) and, in a stratified flow, is necessarily coupled with the scalar (density) transport given by (2.3)

$$\frac{\partial \boldsymbol{u}}{\partial t} + \boldsymbol{u} \cdot \boldsymbol{\nabla} \boldsymbol{u} = -\frac{1}{\rho_0} \boldsymbol{\nabla} p + \nu \nabla^2 \boldsymbol{u} - \frac{g}{\rho_0} \rho \boldsymbol{k}, \tag{2.1}$$

$$\boldsymbol{\nabla} \cdot \boldsymbol{u} = 0, \tag{2.2}$$

$$\frac{\partial \rho}{\partial t} + \boldsymbol{\nabla} \cdot (\rho \boldsymbol{u}) = \kappa \nabla^2 \rho. \tag{2.3}$$

In these equations $\boldsymbol{u} = (u, v, w)$ is the three-dimensional velocity field, ρ_0 is a reference density, p is the pressure, g is gravitational acceleration, κ is the thermal diffusivity (constant) and $\boldsymbol{k}$ is the unit normal vector in the vertical direction. The depth of the simulation domain is 10 m and the length of the domain 150 m. This size domain was chosen in order to cover a simulation gap between the laboratory scale, $O(\leq 10$ m), and full field-scale simulations, $O(\geq 1000$ m). Domain resolution of $\Delta x = \Delta z = 0.05$ m in the horizontal and vertical directions, respectively, result in a total of $n_x \times n_y = 2800 \times 200$, or 560 000 total grid points. This resolution, while not resolving all turbulent scales, allows for realistic nonlinear and overturning flow structures to develop. As defined by Kundu, Cohen & Dowling (2008), the Kolmogorov microscale is defined as a function of the turbulent Reynolds number, $Re_T = U_o L_c / \nu$, where U_0 is the velocity amplitude of the wave forcing and $L_c = U_0/\omega$ is the advective length scale of the internal wave, as $\eta_k = L_c Re_T^{-3/4}$, where ω is the forcing frequency. The simulation grid size of 5 cm used in these simulations is 3.7–10.9 times the corresponding pseudo-Kolmogorov microscale range of 4.6–13.4 mm for the range of simulated flows calculated with $\nu = 1 \times 10^{-5}$, see Table 1 for details. Equations (2.1)–(2.3) are computed using the Massachusetts Institute of Technology's General Circulation Model (`MITgcm`) code within the two-dimensional (x, z) domain depicted in figure 1. `MITgcm` is a CFD code that has been extensively used and validated for simulations of stratified geophysical flows (e.g. Legg & Adcroft 2003; Klymak *et al.* 2012; Legg 2014; Musgrave *et al.* 2016).

At the left boundary of the computational domain simulations are forced with a first-mode internal wave given by

$$u(0, z, t) = U_0 \cos(mz) \sin(\omega t), \tag{2.4}$$

where U_0 is the velocity amplitude of forcing, m is the vertical wavenumber corresponding to a mode-1 baroclinic wave with $m = \pi/d$, and u is the velocity component. Waves are

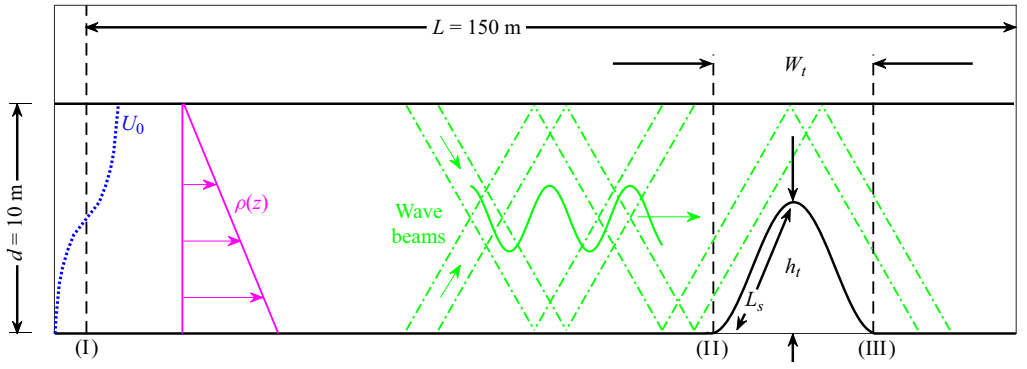

Figure 1. Schematic of the computational domain for the simulations presented. Lines (I), (II) and (III) are the transects where the energy flux was calculated. The height, h_t, and width, W_t, of the topography varied between the simulations dependent on the topography-to-depth ratio, h_t/d and the topographic slope-wave criticality, γ/s. As a result, while the wavelength was set at ∼50 m for all simulations, the width of topography varied between 20 and 70 m, where the slope length is defined by L_s. Simple schematic depictions of the forcing, density stratification and internal wave characteristics are also shown for illustration.

propagated into a domain with an initial stratification (for all simulations) defined using a linear background distribution ρ_b given by

$$\frac{\rho(z, t=0)}{\rho_0} - 1 = \frac{\rho_b(z)}{\rho_0} = -\frac{\Delta\rho}{\rho_0}\left(\frac{z}{d}\right), \tag{2.5}$$

where $\Delta\rho/\rho_0 = 0.0001$ results in a buoyancy frequency $N = 0.01\ \mathrm{s}^{-1}$. In a linearly stratified fluid, as defined for this analysis by (2.5), internal wave phases propagate horizontally at the celerity (speed) defined by

$$c_{ph} = \frac{\omega}{k} = \frac{d}{\pi}(N^2 - \omega^2)^{1/2}, \tag{2.6}$$

where d is the fixed depth, k is the horizontal wave number and ω is the wave frequency. Within this formulation in a stratified flow, the slope of the wave beam, s, is defined by

$$s = \tan\theta = \frac{k}{m} = \left(\frac{\omega^2}{N^2 - \omega^2}\right)^{1/2}, \tag{2.7}$$

where θ is the angle of the internal wave characteristic and m is the vertical wavenumber. Coriolis rotation has been removed from (2.1) and (2.7). While rotation is important to driving oceanic currents and the large-scale eddy structures, it has not been included due to the scale of the simulation being smaller than the scales influenced by rotation. The Rossby numbers ($Ro = U_0/L_c f$) for these simulations are ≈5, which is greater than a Rossby number of 1, indicating that Coriolis rotation should not impact the dynamics in a simulation of this domain size (Galperin *et al.* 1989; Kantha, Rosati & Galperin 1989; Lindborg 2005; Klema *et al.* 2023). The analysis of Phillips (1977) shows that internal waves contain phase-locked downward and upward propagating wave beams where the wave modes propagate horizontally. When an internal wave encounters topography the upward and downward beams decouple and the beams individually interact with the topography and change the dynamics of the flow. The dynamic interaction of the internal waves and topography is impacted by both the slope of the topography, $\gamma = h_t/L_s$, and the wave characteristic slope, s. It is common to see the relative bottom slope defined

by the ratio γ/s. When the topographic slope is steeper than the wave characteristic slope $\gamma/s > 1$, the slope is classified as supercritical. Subcritical slopes correspond to $\gamma/s < 1$ and $\gamma/s = 1$ defines critical slopes. Critical slopes mean that the wave's angle of propagation matches the slope of the topography.

For all simulations a radiative boundary condition (Orlanski 1976) is applied at the right hand boundary to allow for the propagation of the internal wave energy out of the domain; a similar radiation boundary condition is applied in L14, for example. Under some conditions, this boundary condition will allow higher-frequency wave modes to reflect back into the domain. Care was taken with choosing the size of the domain and the test section around the geometry to ensure that the calculations at the ridge were not affected. On the bottom boundary a no-slip boundary condition is applied. At the top of the domain a linearized free surface boundary condition is applied that allows non-zero vertical motions (denoted η), which results in a contribution to the pressure from the boundary displacement. The density field has a gradient-free boundary condition on all walls. A Prandtl number of $Pr = 1$ for all simulations is set by prescribing a kinematic viscosity of $\nu = 10^{-5}$ m^2 s^{-1} and a thermal diffusivity of $\kappa = 10^{-5}$ m^2 s^{-1}. Setting these values for the kinematic viscosity and thermal diffusivity near to the accepted molecular values allows for the large energy containing flow structures to be resolved similarly to a CFD LES, where this slightly higher viscosity than normal will dissipate the eddying structures near the grid scale. No hyperviscosity was used in the simulations, and numerical stability of each simulation was achieved through optimization of the grid size and time step in consideration of the Courant–Friedrichs–Lewy condition. In order to maintain numerical stability the time step varied for each individual simulation, resulting in a range of computational resources used to complete each simulation. The average computational cost across all 40 simulations was 9000 core hours. The maximum computational cost for a single simulation was 12 200 core hours.

Table 1 gives the details of the simulations completed in this analysis, where different values of the topographic slope for different simulations allowed for variation of γ/s from 0 to 1.5 while holding N, ω and s at fixed values. The ratio of ω to N is a scaled quantity and the individual values were chosen such that $N > \omega$ as well as to maintain realistic values for the other parameters in the simulations. The range of subcritical-to-supercritical slopes was achieved by variation of γ using the topographic ridge height, h_t, resulting in a change to the corresponding width, W_t. The relative topographic height h_t/d ranged from 0.25 to 0.75. The ridge geometry is calculated as a function of height from the bed and is defined by the equation $h = (d/2)[1 + \cos((2\pi x - 6\pi\lambda_x)/W_t - \pi/2)]$, where x is the horizontal location from the start of the topography and λ_x is the horizontal wavelength of the internal wave. Velocity amplitude is varied between 0.3 and 2.5 cm s^{-1}, resulting in Froude numbers ($Fr = U_0/c_{ph}$) between 0.1 and 0.84. This definition of the Froude number is the ratio between the velocity amplitude of the wave forcing, U_0, and the internal wave celerity, c_{ph}, and is commonly referred to as the wave Froude number (Venayagamoorthy & Fringer 2007; Legg 2014). This parameter space represents a wide range of wave energy conditions and allows for assessment of various conditions resulting from linear to highly nonlinear internal waves interacting with the topography. A schematic of the computational domain and the relevant parameters associated with the simulation domain are shown in figure 1. The third parameter in table 1 is commonly referred to as the excursion number and is a measure of the wave excursion to the topographic length scale L_s, where T is the internal wave period. This parameter is also sometimes used as a measure of barotropic tide generation.

Runs	γ/s	$Fr = U_0/c_{ph}$	$U_0T/\pi L_s$	h_t/d	$Re_T = U_0L_c/\nu$	η_k (mm)	Comments
1–5	0	0.1–0.84	—	—	260–17 960	13.4–4.6	No-topography cases
6–8	0.25	0.1–0.84	0.03–0.27	0.5	260–17 960	13.4–4.6	Subcritical cases
9–11	0.5	0.1–0.84	0.06–0.52	0.5	260–17 960	13.4–4.6	Subcritical cases
12–16	1	0.1–0.84	0.12–1.03	0.5	260–17 960	13.4–4.6	Critical cases
17–19	1	0.25–0.84	0.62–2.06	0.25	1600–17 960	8.4–4.6	Critical cases
20–23	1	0.5–0.84	0.24–0.67	0.75	6430–17 960	6.0–4.6	Critical cases
24–26	1.25	0.1–0.84	0.29–2.43	0.25	260–17 960	13.4–4.6	Supercritical cases
27–29	1.25	0.1–0.84	0.15–1.21	0.5	260–17 960	13.4–4.6	Supercritical cases
30–32	1.25	0.1–0.84	0.1–0.81	0.75	260–17 960	13.4–4.6	Supercritical cases
33–35	1.5	0.1–0.84	0.33–2.78	0.25	260–17 960	13.4–4.6	Supercritical cases
36–38	1.5	0.1–0.84	0.17–1.39	0.5	260–17 960	13.4–4.6	Supercritical cases
39–40	1.5	0.5–0.84	0.56–1.39	0.75	6430–17 960	6.0–4.6	Supercritical cases

Table 1. Details of the 40 simulations showing the parameter space covered.

3. Results and discussion

3.1. *Velocity and temperature/density fields*

Time series snapshots of internal wave propagation through the computational domain are shown in figure 2. Three simulation cases are shown in this figure for $Fr = 0.1$, $Fr = 0.5$ and $Fr = 0.84$, depicting linear, nonlinear and highly nonlinear cases, respectively. Values for the relative slope $\gamma/s = 1$ (i.e. critical slope) and topography-to-depth ratio $h_t/d = 0.5$ are consistent for the simulations depicted. Also, for all three simulations, the frequency of the incoming internal wave is $\omega = 0.0035$ rad s^{-1} and the wave period $T = 2\pi/\omega = 1800$ s. Forcing of the internal wave is modified by imposing varied velocity amplitude U_0 at the inlet of the domain. Each of the three cases in figure 2 shows six snapshots of the internal wave developing and propagating over the topographic ridge. The time instants are normalized by T. The domain depicted starts at $x = 50$ m, ends at the computational domain outlet $x = 150$ m and is coloured by the stratification, depicted using the temperature anomaly.

With $Fr = 0.1$ the six panels in figure 2(*a*) show the propagation of an internal wave forced by $U_0 = 0.3$ cm s^{-1}. The dynamics of this simulation is dominated by linear oscillations of the flow field as the internal wave propagates to the ridge. Some minimal magnitude displacement is visible in the flow field on the upstream side of the ridge as well as above the peak in topography. While some dissipation and mixing occurs due to the criticality of the topography, a greater portion of the energy is either transmitted past the topography or reflected off the topography. Most of the small-scale features visible in this series of visualizations are a result of the slope criticality leading to the decoupling of the internal wave beams. In the simulations with $Fr = 0.1$ and sub- or supercritical slopes, these features are lesser in extent. As the Froude number increases these features also become less observable as the beam decoupling gets overwhelmed by the energy and the resulting nonlinear dynamics.

Figure 2(*b*) shows a simulation with $Fr = 0.5$ set by $U_0 = 1.5$ cm s^{-1}. The presence of nonlinear dynamics is visible in the snapshots of this simulation with dense fluid from the base of the stratified water column propagating up and over the ridge (see panels (iv) and (v)). These flow structures have been both simulated (Venayagamoorthy & Fringer 2006, 2007) as well as observed (Cacchione & Wunsch 1974) and are known as tidal bores, or solibores. These flow structures are formed as a result of the internal wave creating a

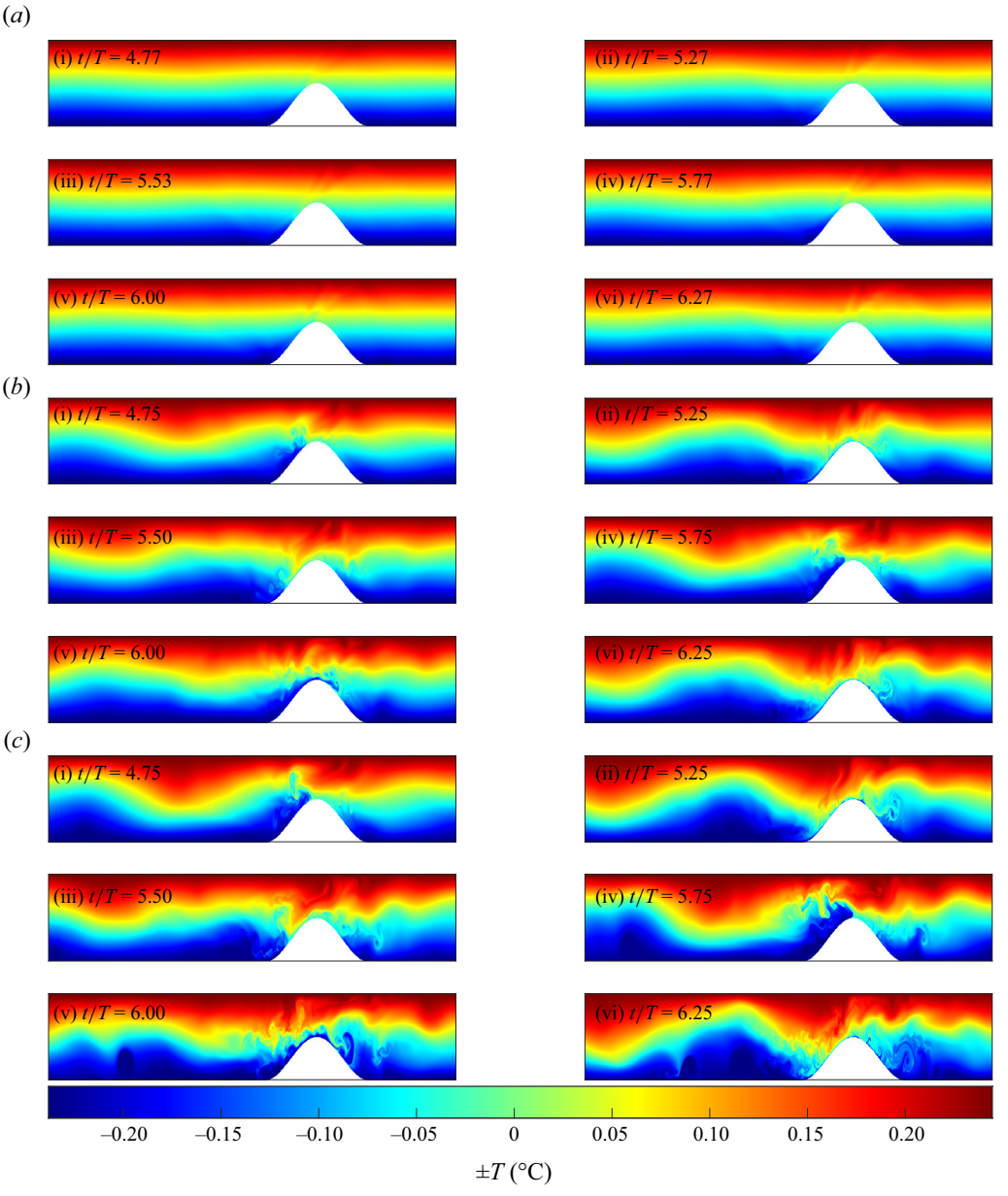

Figure 2. Time series snapshots of an internal wave building and passing over the topographic ridge. Colour spectrum denotes the temperature anomaly of the simulations. The relevant parameters for the simulations depicted are $\gamma/s = 1$, $h_t/d = 0.5$ for (*a*) $Fr = 0.1$, (*b*) $Fr = 0.5$ and (*c*) $Fr = 0.84$. As the Froude number increases the dynamics of the internal waves' interaction with the topographic ridge becomes more complex with more overturning and transport of high density fluid from near the bottom boundary up and over the ridge when $Fr = 0.84$. Note that the first 50 m of the domain is truncated in the figures to better visualize flow structures near the ridge.

vortex core that advects dense fluid from low in the water column up onto a continental shelf (as shown in VF06 for example) or over the top of ridge (as shown here). In addition to the advection of dense fluid by bores, larger magnitude displacements of fluid are visible

relative to the case with $Fr = 0.1$. Displacements of fluid, both on the upstream side of the ridge as well as above the topographic peak, increase in magnitude. The drawdown of fluid on the upstream side of the ridge as the internal wave advects toward the ridge, as well as the propagation of the bore to the downstream side of the ridge, creates regions of unstable stratification where denser fluid overlies less dense fluid. Visible in the snapshots are the overturning structures that result from unstable stratification and the advection of the bolus.

A velocity amplitude of forcing $U_0 = 2.5$ cm s^{-1} sets a simulation with $Fr = 0.84$, depicted in figure 2(*c*). It is clear from the series of snapshots that the dynamics becomes highly nonlinear with significant instability with the increase in energy. Fluid displacements, the size of the bore transporting mass over the ridge as well as the size of the overturns resulting from unstable stratification are all of greater magnitude when compared with the other two cases. In the case shown in figure 2(*b*) the bore is ejected off the ridge, creating an overturn and mixing. In this case, the size/mass of the bore is sufficiently large that it returns down the backside of the ridge. This downslope advection of the bore (as shown in figure 2*c*-v) generates an overturning structure that is in the opposite direction to the ejected bore depicted in figure 2(*b*-v). This final time series clearly shows the complex dynamics that results from highly nonlinear internal waves interacting with topography in a stratified flow.

Figure 3 shows the normalized zonal velocity u, normalized vertical velocity w and normalized density profiles for the same three cases discussed for figure 2 at $t/T = 6.25$. Figure 3(*a*) shows profiles for $Fr = 0.1$, figure 3(*b*) for $Fr = 0.5$ and figure 3(*c*) for $Fr = 0.84$. Each row of normalized plots correspond to transects I-III as depicted in figure 1, respectively. The zonal velocity, vertical velocity and density profiles at profile § 1 in the first row for each of the cases show a similar distribution as expected but normalization of the velocities by U_0 results in varied magnitudes due to the differences in the velocity amplitude of forcing.

For the linear lowest energy case ($Fr = 0.1$) the profiles at transect II show a zonal velocity distribution with increased values near the bed as the wave approaches the ridge. The vertical velocity magnitude at transect II has also increased, as would be expected with the zonal flow being redirected vertically over the ridge. The density profile steepens near the bed, likely due to the energy of the internal wave pushing the dense fluid near the bottom against the base of the ridge and creating a slight increase in the density near the bottom of the profile. Row 3 of panel (*a*) shows the distributions of transect III, the downstream side of the ridge. Both the zonal and vertical velocity magnitudes have decreased. On the lee side of the ridge the zonal velocity should decrease as it is sheltered from the incoming internal wave and the vertical velocity switches direction as some of the flow moves down the back side of the ridge.

Figure 3(*b*) shows the normalized velocity and density profiles at transects I, II & III for simulation with $Fr = 0.5$ at $t/T = 6.25$. At transect II the normalized zonal velocity shows a velocity distribution representative of the drawdown on the upstream side of the slope just before the arrival of an internal wave. This distribution is corroborated by the corresponding image from figure 2(*b*-vi) showing the fluid being drawn downslope during the simulation at this instant, resulting in the negative vertical velocity. The density profile also shows the impact of the drawdown of lighter fluid from higher in the stratified fluid column.

In figure 3(*c*) similar trends are observable for the simulation defined by $Fr = 0.84$ at $t/T = 6.25$. The increased velocity of this simulation results in a zonal velocity distribution that is already propagating up the ridge at transect II. It had not yet arrived

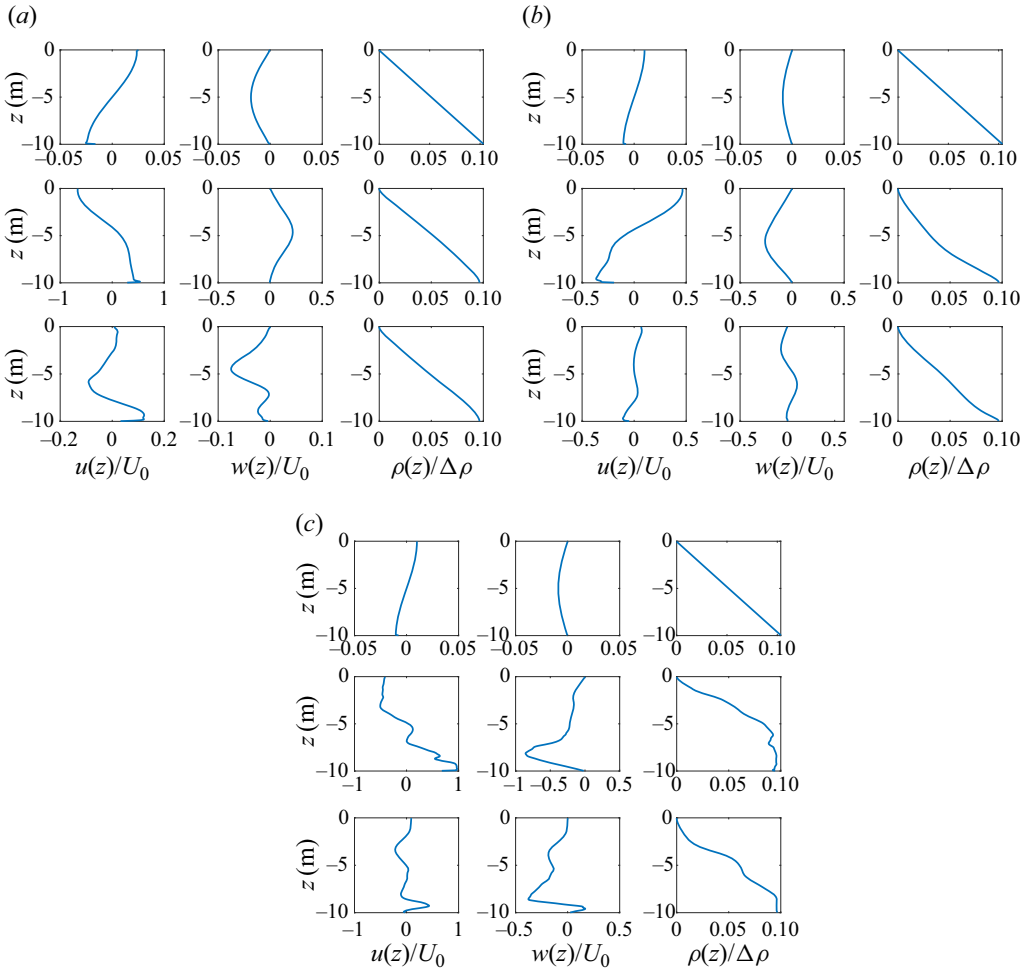

Figure 3. Normalized zonal velocity (u), vertical velocity (w) and density (ρ) profiles for $t/T = 6.25$. Grouping (a) is for simulation where $Fr = 0.1$, grouping (b) $Fr = 0.5$ and (c) $Fr = 0.84$. The other relevant parameters are $\gamma/s = 1$ and $h_t/d = 0.5$ for all three simulations. Within each grouping row 1 denotes the profile from transect I, row 2 the profile from transect II and row 3 from transect III on the downstream side of the topographic ridge as depicted in the schematic shown in figure 1.

at the ridge in the previous case, resulting in the drawdown profile discussed above. The density profiles from transects II and III show the result of the increase in energy of this simulation with more varied distributions of density due to turbulence and mixing. Regions of unstable stratification are also observed in the density profile at transect II. The flow structures visible in all three of the simulation time series shown in figure 2 are signatures of nonlinear as well as non-hydrostatic effects. These nonlinear structures are sufficiently resolved in the current simulations to be visible within the flow, similar to those seen in highly resolved simulations such as in VF06.

3.2. *Energy flux and partition*

Here, we repeat a concise portion of the derivation for the depth-integrated energy flux presented in VF06 and Venayagamoorthy & Fringer (2005) but it will be applied here

to a topographic ridge rather than a shelf. This analysis is also similar to the derivation presented in Rapaka *et al.* (2013) for the energy flux components and the determination of relative energy transmission, reflection and dissipation. Taking the dot product of (2.1) with $\boldsymbol{u}$ and adding the resulting equation to the product of (2.3) and gz gives the governing energetics equation

$$\frac{\partial}{\partial t}(\rho_0 q + \rho g z) + \boldsymbol{\nabla} \cdot \boldsymbol{f} = -\rho_0 \epsilon_k - 2\kappa \frac{\partial}{\partial z}(\rho g), \tag{3.1}$$

where $q = \boldsymbol{u} \cdot \boldsymbol{u}/2$ is the kinetic energy per unit mass, $\epsilon_k = \nu((\partial u_i/\partial x_j)(\partial u_j/\partial x_i))$ is the viscous dissipation rate of kinetic energy and the local energy flux is given by

$$\boldsymbol{f} = \boldsymbol{u}(\rho_0 q + p + \rho g z) - \mu \boldsymbol{\nabla} q - \kappa(\rho g z), \tag{3.2}$$

with μ denoting the dynamic viscosity. From the equations derived above it follows that the depth-integrated energy flux (units of W m^{-1}) is given by

$$F_E = \int_{-d}^{0} \left[u(\rho_0 q + \rho g z + p) - \mu \frac{\partial q}{\partial x} - \kappa \frac{\partial}{\partial x}(\rho g z) \right] \mathrm{d}z. \tag{3.3}$$

Assuming that at $t = 0$ the density field is given by the imposed background density field ρ_b and that the contribution of the diffusive terms to the energy flux is negligible, the change in total energy can be computed using the simplified depth-integrated energy flux

$$F_E = \int_{-d}^{0} p' u \, \mathrm{d}z, \tag{3.4}$$

where $p' = \rho_0 q + \rho g z + p$. The time-integrated energy flux (units of J m^{-1}) is given by

$$E_\tau = \int_0^t F_E(\tau) \, \mathrm{d}\tau. \tag{3.5}$$

The pressure term p in (3.3) can be split into two terms denoting its hydrostatic (p_H) and non-hydrostatic (p_{NH}) components gives $p' = \rho_0 q + \rho g z + p_H + p_{NH}$. If the total density is defined by $\rho = \rho_0 + \rho_b + \rho'$, (3.3) can be written to account for the energy flux due to the work done by the hydrostatic pressure fluctuations (*i*), the work done by the non-hydrostatic pressure (*ii*), the advection of kinetic energy (*iii*), the advection of potential energy due to density fluctuations (*iv*), advection of potential energy due to the mean background density field (*v*) and work done by the hydrostatic pressure due to the mean background density field (*vi*). This derivation is analysed in detail, including a discussion of each contributing term, in Venayagamoorthy & Fringer (2005), Kang & Fringer (2010) and Kang & Fringer (2012). Each of the energy flux contributions listed above can be determined from the numerical simulation data that are included explicitly as part of the simulation. The analysis presented in Kang & Fringer (2012) (among others) shows that terms (*iv*)–(*vi*) minimally contribute to the overall energy flux and these findings were corroborated in our analysis. The results of VF06 show that over 50 % of the energy flux results from the hydrostatic pressure anomaly while approximately 30 % of the energy flux is contributed by the non-hydrostatic pressure term, the two largest contributors to the energy flux budget in their analysis. Figure 4 shows both the depth-integrated flux (solid blue lines) as well as the cumulative energy flux (dashed magenta lines) for each of the three largest flux contribution terms (*i*)–(*iii*) for simulations where $Fr = 0.1$, $Fr = 0.5$ and $Fr = 0.84$ with $\gamma/s = 1$ and $h_t/d = 0.5$ in all

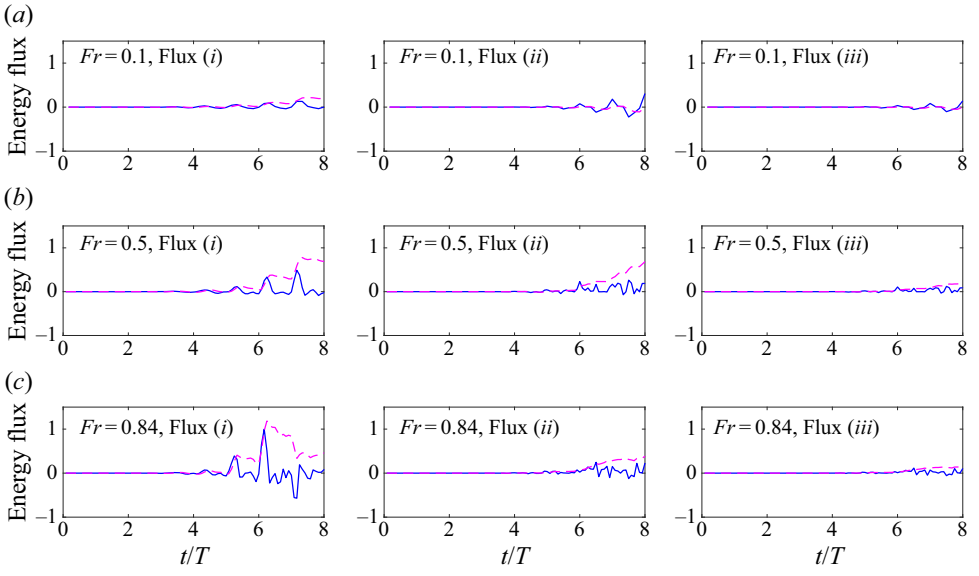

Figure 4. Depth-integrated energy flux normalized by F_L (blue solid line) and time-integrated (cumulative) energy flux normalized by F_L/ω (magenta dashed line) as a function of t/T at $x = 105$ m for simulations with $Fr = 0.1$ (*a*), $Fr = 0.5$ (*b*) and $Fr = 0.84$ (*c*). These are the same simulations as presented in figure 2, with $\gamma/s = 1$ and $h_t/d = 0.5$ consistent between simulations. The calculations are as in transect III on the downstream side of the ridge as denoted in figure 1.

three simulations. For the higher Fr simulations shown in figure 4, the hydrostatic pressure anomaly term accounts for approximately 50 % of the energy flux and the non-hydrostatic pressure term approximately 35 %–40 % of the total energy flux. Each energy flux term plotted in figure 4 is normalized using a base estimate of the energy flux of the incoming internal wave computed using linear wave theory (Kundu *et al.* 2008)

$$F_L = \frac{\rho_0 \omega U_0^2}{2k} d, \tag{3.6}$$

where ρ_0 is the reference density, ω is the forcing frequency, U_0 is the velocity amplitude of forcing, d is the full flow depth and k is the horizontal wavenumber obtained from the dispersion relation for internal waves. This energy flux is the integral of the product of the velocity and pressure perturbations. The evident contribution of the non-hydrostatic pressure work term shows the impact of vertical inertia and the instantaneous importance of the non-hydrostatic pressure. This figure shows that, as the Froude number increases, both the hydrostatic and non-hydrostatic energy fluxes increase. This result corroborates the laboratory-scale results of VF06 and illustrates the importance of the non-hydrostatic dynamics in stratified flows and internal wave CFD simulation.

Using the notation presented by VF06, the energy budget can be approximated by

$$E_I = E_R + E_T + E_D, \tag{3.7}$$

where E_I is the total incident wave energy of the incoming wave, E_R is the energy reflected back toward the inlet of the computational domain from the topography, E_T is the energy transmitted past the topography and E_D is the energy dissipated in the control volume bounding the topography. Figure 5 shows a schematic depiction of the components of the energy flux budget with the control volume centred over the topography between

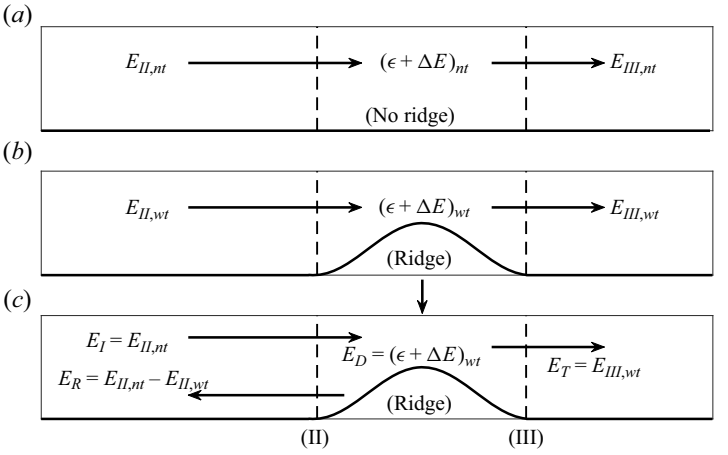

Figure 5. Depiction of the energy budget for the control volume centred over the topographic ridge between vertical transects II and III. Panel (*a*) shows the base case where no topography is present ($\gamma/s = 0$) and panel (*b*) shows the typical topographic ridge case ($\gamma/s > 0$). Schematic (*c*) shows how the fluxes are determined from panels (*a*) and (*b*) to close the energy budget and determine the reflected and dissipated energy. Subscript '*nt*' denotes the no-topography case and '*wt*' denotes the case with a topographic ridge (modified from Venayagamoorthy & Fringer (2006), not to scale).

the dashed lines denoting transects II and III as show in figure 5. The reflected energy flux is determined by taking the difference in the total incident wave energy flux of transect II (see figure 5(*a*)) of the simulation with no topography present, $(E_\tau)_{nt,II}$, and the total wave energy flux that now includes both incident and reflected wave energies at transect II (see figure 5(*b*)) in the simulation with the topographic ridge being evaluated, $(E_\tau)_{wt,II}$. Dissipation of energy is determined from (3.7) by taking the difference between the cumulative total wave energy flux of transect II and the cumulative energy flux of transect III.

Analysis of how the energy is partitioned between these three components across a wide range of pertinent parameters (i.e. Fr, γ/s and h_t/d) will be insightful for understanding the dynamics of the interaction process and is carried out next.

Figure 6 shows the cumulative transmitted, reflected and dissipated energy fluxes for each simulation as a function of γ/s, for $h_t/d = 0.25$, 0.5 and 0.75, respectively. All the fluxes are normalized by the cumulative incident energy E_I. When the ridge height is only one quarter of the total flow depth, $h_t/d = 0.25$ (figure 6*a*,*d*,*g*), the majority of the incident wave energy (approximately 70 %) is transmitted through the domain at the critical slope and reduces monotonically to approximately 50 % for $\gamma/s = 1.5$. The amount of energy reflected is very small for the critical slope cases (regardless of Fr) but increases slightly when the slope becomes supercritical, offsetting some of the reduction in transmitted energy. The dissipation accounts for the remainder of the incident energy that is not transmitted at critical slopes and slightly increases for supercritical slopes especially for $Fr = 0.84$.

The second column of figure 6 shows the results for a ridge height $h_t/d = 0.5$. Subcritical slope simulations allow for the majority of the energy to transmit up and over the topography but some energy is dissipated by turbulence in the flows with higher Froude numbers. The transmitted energy decreases in a monotonic manner as γ/s increases regardless of Fr, similar to the trend seen in VF06. Amounts of reflected energy are very small, as would be expected as the internal wave beams forward reflect when the

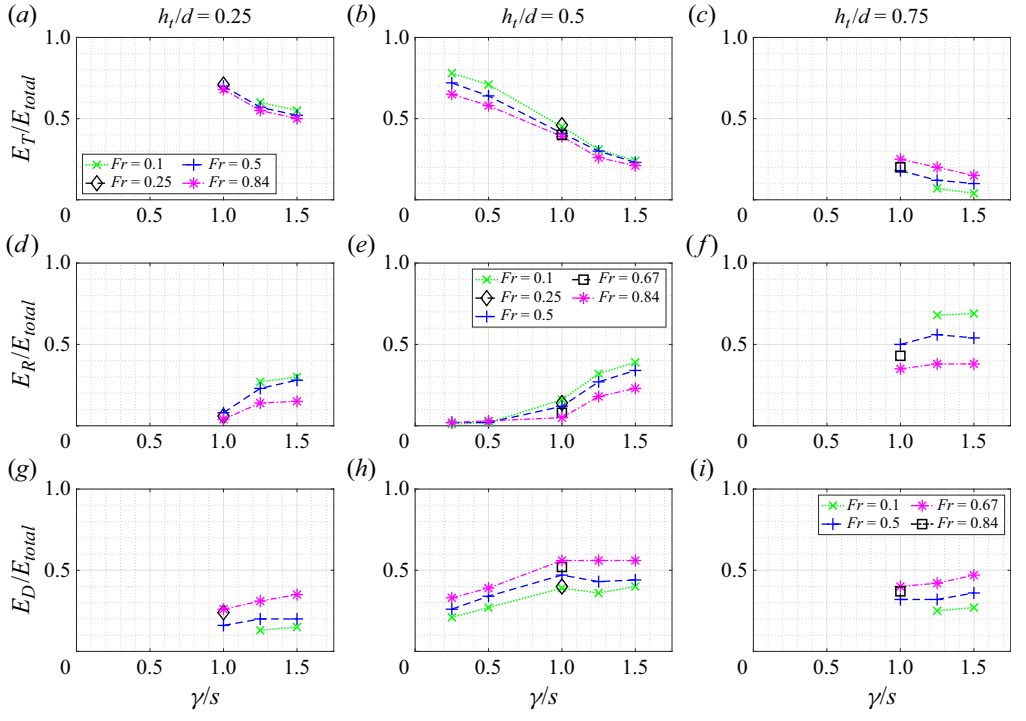

Figure 6. Normalized cumulative energy fluxes for all simulation runs as a function of the topographic steepness parameter. Rows denote the normalized transmitted energy flux, normalized reflected energy flux and normalized dissipated energy flux, respectively. Columns group the results by the topography height–total depth ratio, h_t/d.

slope is subcritical. For critical slopes approximately half of the energy is transmitted. The amount of reflected energy remains the least significant of the three energy modes analysed in the cases with critical slopes. However, for supercritical slopes, reflection increases significantly, reaching almost 40 % at $\gamma/s = 1.5$. Both the proportions of transmitted and reflected energy are always higher for the lower Fr cases for all γ/s values, a result also seen in VF06. Dissipation magnitude varies as a function of Froude number, with dissipation accounting for approximately 50 % of the energy difference at high Froude numbers at critical slopes to less than 25 % for the lowest Froude number simulation, $Fr = 0.1$ for subcritical slopes.

As the height of the ridge increases the amount of transmitted energy also decreases, as shown in figure 6(*c*). Approximately 25 % of the energy is transmitted for a ridge defined by a critical slope and the majority of the energy is reflected. For the least energetic simulations defined by $Fr = 0.1$ the amount of energy transmitted through the domain is very low, with over 70 % of the energy being reflected off the topography and the majority of the difference being dissipated. Amounts of reflected energy vary significantly with Fr, with total reflected energy decreasing as Froude number increases. Flows defined by a larger Froude number lead to a more nonlinear dynamics and more of the energy being captured by dissipation and mixing. The plots in figure 6 show how the partition of energy flux is strongly dependent on all three non-dimensional parameters Fr, h_t/d and γ/s.

On average 43 % more of the total wave energy is transmitted through the domain when $h_t/d = 0.25$ than when $h_t/d = 0.75$. The amount of the total wave energy that is

reflected for these two cases is almost inversely proportional, with 36 % more energy being reflected on average for the simulations with $h_t/d = 0.75$ when compared with the amount of energy reflected from simulations with $h_t/d = 0.25$. The amount of energy dissipated is 16 % higher on average for $h_t/d = 0.75$ than $h_t/d = 0.25$, which can be attributed to the increased length of the wave-to-bed interaction that results from the increasing height of the topography. Results with $h_t/d = 0.5$ necessarily fall in the middle of the range in terms of wave energy transmission, reflection and dissipation. Results from this subset of simulations with $h_t/d = 0.5$ clearly illustrate the influence of γ/s. There is an average decrease of 40 % of the total wave energy transmitted as γ/s increases (i.e. from subcritical to supercritical slopes). Results show that, for $h_t/d = 0.5$, there is an average 31 % increase in the amount of total wave energy reflected with increasing γ/s. Total wave energy dissipated increases by 16 % with increasing slope steepness and the amount of wave energy levels off at approximately 50 % after reaching a critical slope.

If the results presented in figure 6 are directly compared with the results in VF06 there are a few notable differences. The two results are not directly comparable due to the different simulation scales, a shelf being used in VF06 as compared with a topographic ridge here and the different parameter value ranges explored (*Fr*, wave parameters etc.). In particular, it should be noted that, in VF06, the topographic steepness and topographic height were not independently varied, making a direct comparison difficult. Nonetheless, comparisons between the two studies taken on an average basis show decreases in transmission of 4 %. This decrease in transmission can be partially explained as a result of the longer overall bottom length travelled by the internal wave while going over the topographic ridge as opposed to travelling along the shelf. Additionally, the potential energy contained by bolus mass cores at the top of the ridge is converted to kinetic energy as the bolus is ejected and plunges off the top of the ridge. A significant component of this kinetic energy that is not present in the shelf case in VF06 is in the vertical direction, contributing to additional mixing. There is an increase in the average reflection of 5 % and a decrease in the dissipation by 2 %. Increases in reflection are a result of the some of the resulting re-circulations observed in these simulations that move fluid mass back past the upstream toe of the ridge. The dissipation makes up the necessary difference.

Data presented in figure 7 depict a subset of the overall data presented in figure 6 at the critical slope ratio, $\gamma/s = 1$. The proportions of transmitted, reflected and dissipated amounts of energy are presented on the horizontal axis and the ridge height-to-depth ratio on the vertical axis in order to maintain this quantity's physically realistic orientation. Each data point is coloured by *Fr* of the simulation. Figure 7(*a*) shows that the transmitted energy flux decreases linearly with h_t/d at the critical slope. As nicely discussed in L14, in the near-critical slope regime, it can be shown that, for a finite-length critical slope with a piecewise constant slope (e.g. a triangular ridge), the fraction of energy flux that will be transmitted scales linearly with $(1 - h_t/d)$. The agreement, as shown by the dashed line in figure 6(*a*), with the simulation results is remarkable despite the differences in shape of the topography and variations in *Fr*. This finding is also corroborated in the field-scale simulations of L14, where a similar monotonic decline in transmitted energy with h_t/d is seen at critical slopes. However, there are some changes with *Fr* that are worth noting. At $h_t/d = 0.25$, the effect of *Fr* is small with slightly less transmission at higher *Fr*. At $h_t/d = 0.5$, the effect of *Fr* increases in a non-monotonic manner with the peak transmission ratio of approximately 0.5 at an intermediate $Fr = 0.25$. Such a non-monotonic trend in the transmission ratio with *Fr* for a critical slope was also found in VF06, wherein they report a value of approximately $Fr = 0.34$ at peak transmission. Figure 7(*b*) shows that the proportion of reflected energy increases with ridge height in

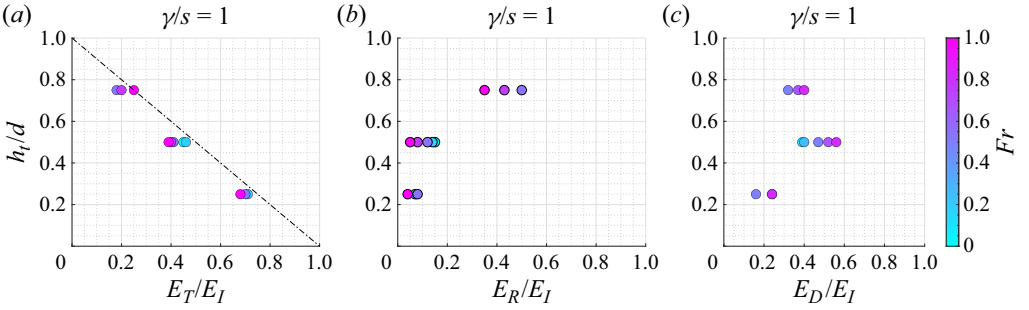

Figure 7. Energy transmission, reflection and dissipation for the three ridge heights at $\gamma/s = 1$. Energy transmission increases as the ridge height decreases, panel (*a*), energy reflection increases with increases in ridge height, panel (*b*), and energy dissipation peaks for the intermediate ridge height, panel (*c*). The linear trend line in panel (*a*) directly follows from linear theory, as presented in L14, of $E_T/E_{total} = 1 - h_t/d$.

a highly nonlinear manner. The increase in reflected energy is only slight (approximately 10 %) between the cases with $h_t/d = 0.25$ and 0.5. On the other hand, the increase is drastic when h_t/d changes from 0.5 to 0.75. Given the linear trend in the transmitted energy, it is clear that dissipation is significant at $h_t/d = 0.5$. Figure 7(*c*) shows that the dissipation exhibits a non-monotonic behaviour with a peak at the intermediate ridge height for critical slopes. Even though there is a longer surface for the wave to traverse in the cases of the taller ridges, this result is likely a result of the scale of incoming wave energy and the scale of the topographic 'obstacle', where the amount of energy dissipated decreases for the taller ridge. This finding has important implications for optimal mixing 'hotspots' in the ocean.

The simulation snapshots presented in figure 8 qualitatively depict this interaction between the wave and topography. The first row of panels, (*a–c*), depicts the same time snapshot of the simulations for $Fr = 0.5$ and $\gamma/s = 1$ at all three ridge heights. For the smallest ridge depicted in figure 8(*a*) there is clearly some nonlinear fluid dynamics, as shown by some overturning structures with denser fluid moving up over the ridge. In figure 8(*b*) the bolus core of fluid ejected over the ridge is larger, but it is also clear that there is an increase in the nonlinear dynamics with more visible mixing between the layers of fluid. In the case of the tallest ridge, the scale of the incoming wave does not match the scale of the topography so the bolus size decreases and the densest fluid is not able to go over the top of the ridge.

If the simulation Froude number is increased to 0.84 this same result holds. At the intermediate ridge height, the bolus structures increase in size from the $Fr = 0.5$ case with the same ridge height, as can be seen in figure 8(*e*). For the tallest ridge (see figure 8*f*), there is also an increase in the bolus size and the amount of mass ejected over the ridge when compared with the same ridge height at $Fr = 0.5$. However, when compared with the intermediate ridge height case at $Fr = 0.84$ (figure 8*e*), there remains insufficient wave energy to move the densest fluid over the ridge. Figure 8(*d*) gives a similar presentation of the data as figure 7(*a*) for the transmission of wave energy but for all γ/s values and ridge heights. Data are still coloured by simulation Froude number. Similar to the relationship between E_T/E_{total} and h_t/d, the relationship between γ/s and E_T/E_{total} follows a linear relationship for all of the data. The trends in the transmitted energy are different with respect to Fr and h_t/d. For $h_t/d = 0.25$ and $h_t/d = 0.5$ the amount of energy transmitted decreases with increasing Fr. This energy is being absorbed in the energy dissipation for each constant ridge height across all γ/s. For $h_t/d = 0.75$ a similar linearly proportional

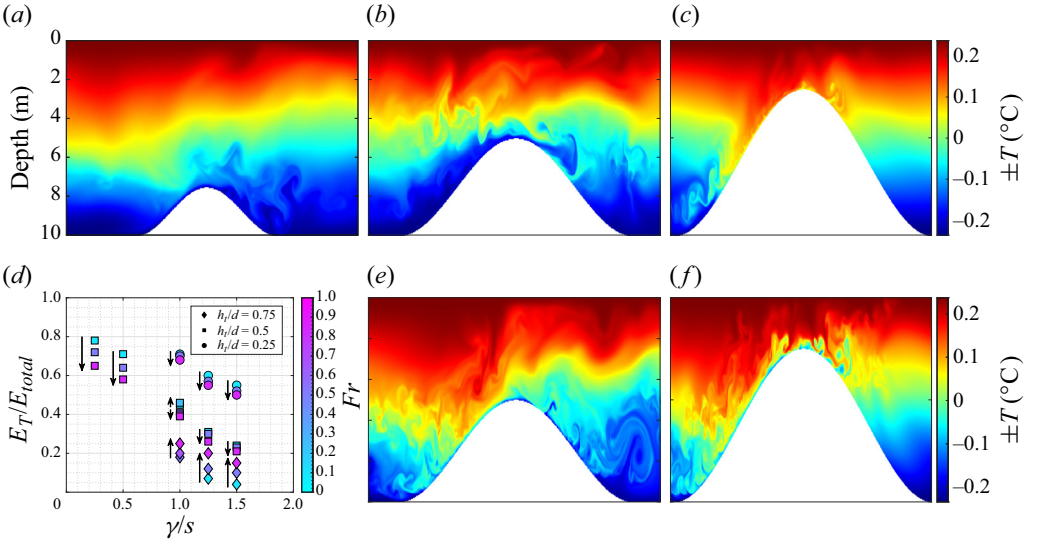

Figure 8. Panels (*a–c*) show a snapshot of internal wave interaction with topography for the three ridge heights all at $Fr = 0.5$ and $\gamma/s = 1$. Panels (*e–f*) show internal wave interaction with $h_t/d = 0.5$ and $h_t/d = 0.75$, respectively, for $Fr = 0.84$, $\gamma/s = 1$. Panel (*d*) presents the energy transmission trends with respect to γ/s, h_t/d and Fr, where there is a clear, nearly linear trend in the decrease of transmitted energy as ridge height increases. For $h_t/d = 0.25$ and $h_t/d = 0.5$ the amount of energy transmitted decreases as the Froude number increases due to an increase in dissipation but it is worth noting the reverse Fr trend for simulations with $h_t/d = 0.75$ as more energy is needed to overtop the ridge.

relationship between γ/s and E_T/E_{total} as the other two ridge heights occurs, but the amount of energy transmitted as a function of Fr has the opposite trend, as shown in figure 8(*d*). For the taller ridges, increase in Fr provides more wave energy to transmit energy over the tallest ridges and in balance appears to have the impact of reducing the amount of energy dissipated, as shown in figure 6(*i*).

Figure 9 shows both a reproduction of the regime diagram presented as figure 2 in L14 and a series of simulation snapshots with various values of γ/s. The regime diagram, presented on the left side of the figure, depicts the parameter space defined by the relative topographic height and the slope ratio. All simulations completed in this study are superimposed on this reproduced diagram. Regions A and C are defined by subcritical topographic slopes. Regime region B is the near-critical slope region and the simulations presented in this study overlap with the simulations completed in L14 in these regimes. The bounds of region B are delineated by α_1 and α_2, where $\alpha_1 = (1 - \sqrt{Fr})/(1 + \sqrt{Fr})$ and $\alpha_2 = (1 + \sqrt{Fr})/(1 - \sqrt{Fr})$. As defined in L14, Fr is the initial Froude number of the simulation. Region D is dominated by lee-wave generation and region F is defined by very small topography relative to the internal wave height and neither of these parametric regime spaces were investigated in this study. This study fills a simulation regime gap that has received less attention by completing simulations in the intermediate region E. In this highly supercritical regime, the waves will transition from being dominated by wave breaking toward lee-wave generation. Panels (*c*) and (*f*) in figure 9 show that, even for $\gamma/s = 1.5$, there are still overturns generated from the internal wave–topography interaction and the regime has not yet transitioned. Resolution of the vertical velocity field and the non-hydrostatic contribution help these nonlinear features develop and may not be well accounted for in simulations that neglect the non-hydrostatic contributions and/or

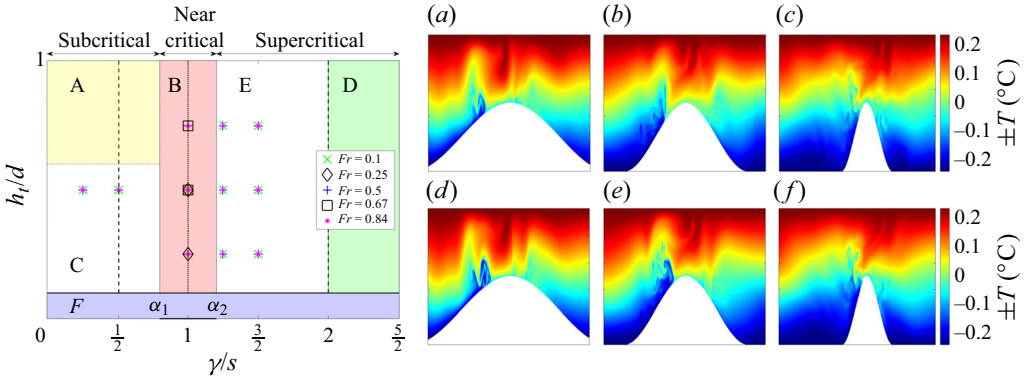

Figure 9. On the left side of the figure is a reproduction of the regime diagram shown in L14 figure 2, where the locations of the numerical experiments performed by this study are overlaid on the regime diagram for context. Panels (*a–f*) on the right side of the figure show simulation snapshots at $h_t/d = 0.5$ but for a range of γ/s values and two values of the Froude numbers. Panels (*a–c*) show results with $Fr = 0.5$ and with γ/s values of 0.25, 0.5 and 1.5, respectively. Panels (*d–f*) show the same iteration values for γ/s but at $Fr = 0.84$.

have an insufficient grid resolution. Regime D in the reproduction of the L14 diagram in figure 9 has been studied previously (e.g. Laurent *et al.* 2003; Klymak *et al.* 2013) and presents the 'knife edge' ridges having highly supercritical slopes. In Klymak *et al.* (2013) the dissipation is concentrated near the peak of the ridges studied and is a result of the interaction/scattering between different modes of the internal tide and topography. While our cases are not directly comparable due to different regimes as well as a large difference in Froude number, it is clear from the present study that non-hydrostatic effects are important and result in mixing near the base of the ridge where a significant portion of the nonlinear structures are generated and interact, just beyond the crest of the ridge. The other result of note is that the simulations in figure 9(*a*,*b*,*d*,*e*) show internal wave overturning and breaking where such would not be predicted by the analysis in L14. This is a result of two distinct differences from the simulations in L14. First, the high-resolution simulations at these intermediate scales allow for non-hydrostatic effects to be modelled more precisely when compared with lower-resolution simulations that appear to minimize the non-hydrostatic contributions, as discussed previously. The simulations presented here also impose a no-slip boundary condition on the bottom boundary of the simulation domain that many field-scale simulations do not due to lack of adequate grid resolution. While these simulations still do not resolve the bottom boundary layer, imposing the no-slip boundary condition also contributes to a change of the flow dynamics that leads to overturning as the internal wave interacts with the bottom boundary and the topographic ridge.

4. Summary and conclusion

Locations with topographic ridges in the Earth's oceans have been identified as hotspots for dissipation and mixing. This parametric study presents an analysis of highly resolved two-dimensional numerical simulations of internal waves with varied velocity amplitude of forcing U_0 encountering topographic ridges with varying height h_t and relative slope criticality γ/s. These parametric variations result in flows characterized by a range of Froude numbers with the correlated flow dynamics varying from conditions dominated by

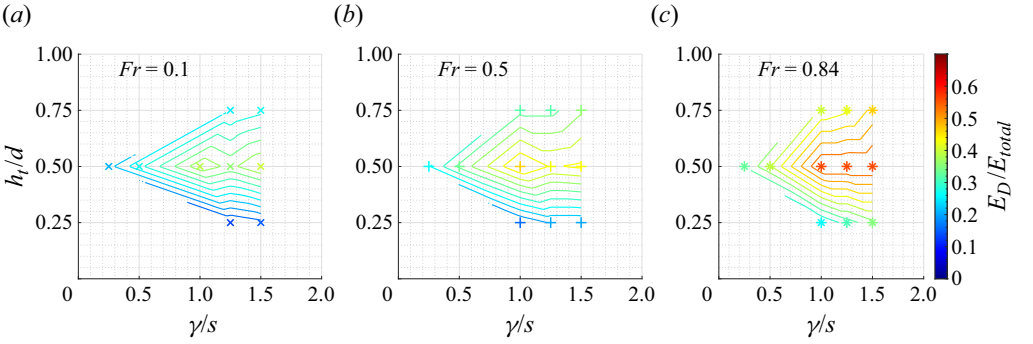

Figure 10. Interpolated contour trends of energy dissipation for all simulations completed in this study at $Fr = 0.1$, $Fr = 0.5$ and $Fr = 0.84$, respectively.

linear oscillations at low values of the Froude number to a complex nonlinear dynamics at high values of the Froude number.

For a ridge topography with subcritical relative slopes ($\gamma/s < 1$) the majority of the available internal wave energy is transmitted as the internal wave beams are forward reflected past the topographic ridge. Differences in the amount of the energy transmitted in the different simulations with a subcritical slope are directly correlated with the internal wave amplitude, however, more energy is lost to dissipation as the amplitude of the internal waves increases ($Fr = 0.67$–0.84). Conversely, for supercritical slope values where $\gamma/s > 1$, the majority of the available energy is back reflected rather than transmitted and the magnitude of dissipation has a similar dependence on the amplitude of the internal wave forcing. As would be expected, more energy is transmitted when the ridge height is only 25 % of the flow depth than when the ridge height is 50 % or 75 % of the flow depth. The magnitude of transmitted energy decreases as the ridge height increases and this holds for both the subcritical and supercritical cases.

For critical slope cases with $\gamma/s = 1$ the rates of energy transmission, reflection and dissipation are even more strongly correlated with the internal wave amplitude. Topography with a critical slope concentrates the wave energy, leading to increased complexity in the flow dynamics, illustrated by the formation and propagation of bolus structures. Inherent flow instability at high Froude numbers leads to increased energy loss due to dissipation as the wave breaks onto the ridge. This loss of energy in the interaction process creates conditions where dense fluid is caught in the structure of the breaking wave and the kinetic energy advects this mass of fluid onto the ridge. In some cases the available energy is sufficient to move dense fluid over the top of the ridge and back down the downstream side, generating enhanced mixing and turbulence in the stratified fluid on the downstream side of the ridge. A key result from this study is the finding that, at critical slopes, the transmitted energy scales as a linear function of the topographic height h_t/d as shown in figure 6(*a*). This is a key insight that can be helpful in energy budget parameterizations for internal wave–topography interactions.

Figure 10 summarizes the overall trend in dissipation for all simulations completed for $Fr = 0.1$, $Fr = 0.5$ and $Fr = 0.84$. While the full parametric space presented in this figure has clearly not been completely explored by this study, important insights from our analysis can be summarized in this figure. While there is clearly greater overall dissipation with increasing Froude number, the relative difference between the minimum and maximum normalized dissipations remains similar at $\sim 30\,\% \pm 5\,\%$ across Froude numbers. The partition of energy between transmitted, reflected and dissipated energy, as discussed

within the analysis of the results, can be observed in this figure. Increasing ridge height and criticality lead to less dissipation due to increased reflection of wave energy, however, as the Froude number increases, the transmitted wave energy will increase at the expense of dissipation. An important result is the plateau of energy dissipation that is evident across all Froude numbers for $h_t/d = 0.5$ and $\gamma/s \geq 1$.

This analysis uses `MITgcm`, a tool validated and trusted for the simulation of stratified flow and internal waves, but where most simulations have been completed using a field-scale topography ($\geq$ 1000 m). Simulation at this scale generally results in a computational grid spacing of the order of tens to thousands of metres. On the other extreme, DNS and LES simulations of internal waves at laboratory scales have a grid size that is sufficiently small to resolve most or all of the turbulent scales but they do not simulate flow that can be directly correlated to field measurements. A significant contribution of this study is that the analysis is completed at an intermediate scale. These results can illuminate information and build confidence in how DNS and LES results can be applied to field-scale simulations. The simulations presented here are not completed at a resolution that is fine enough to resolve the turbulent scales but by careful choice of the parameters and grid resolution we are able to show results corroborating findings of DNS studies without fully resolving the finest scales of the flow. This work aims to start the building of 'bridges' or 'ties' between DNS and field-scale simulations. Resolution matters, but as this analysis shows, a simulation does not need to be DNS to correctly replicate the non-hydrostatic flow features such as overturns and bores that are visible in visualizations of laboratory-scale DNS.

As computational power increases, field-scale simulations could be completed that resolve smaller and smaller scales. Simulations at the intermediate scale that are able to account for the non-hydrostatic influence on the flow, as presented here, are a necessary step to 'bridge' modelling scales until more resolved field-scale simulations are realizable. This analysis shows why it is important to analyse this simulation gap to illustrate the difference in modelling at the two different scales. Two examples show that dissipation drops without resolution of the dissipative (small) scales, as shown in the comparison with VF06, and that the overturning and breaking of internal waves occurs at a lower Froude number than shown by the field-scale simulation presented in L14, where the simulations do not have a no-slip boundary and do not adequately resolve non-hydrostatic velocities.

Without simulations at the intermediate scale. the nuances of changes in the flow field are obfuscated by the large step in simulation scale and large decrease in simulation resolution. Simulations in three dimensions require significantly greater computational resources, therefore, this type of parametric study allows for future three-dimensional simulations to focus on cases that will form the most informative investigation of overturning structures and the resulting dissipation/mixing. In three dimensions there will be increased dissipation, secondary instabilities and a nonlinear dynamics (Fringer & Street 2003), increasing the complexity of the simulation. Additionally, simulation at this scale in three dimensions will allow investigation of different types of topographic structures, such as seamounts or discontinuous ridges, allowing for flow separation and a more complex flow dynamics to be studied.

Acknowledgements. The authors thank the three anonymous referees for their useful comments and recommendations that have helped us to substantially improve the manuscript.

Funding. We gratefully acknowledge funding from the Office of Naval Research (N00014-22-1-2043) and the National Science Foundation under grant no. OCE-2149047.

Declaration of interests. The authors report no conflict of interest.

Author ORCIDs.
Matthew R. Klema https://orcid.org/0000-0002-6605-7232;
Subhas K. Venayagamoorthy https://orcid.org/0000-0001-7895-4144.

References

AGUILAR, D.A. & SUTHERLAND, B.R. 2006 Internal wave generation from rough topography. *Phys. Fluids* **18** (6), 066603.

AGUILAR, D.A., SUTHERLAND, B.R. & MURAKI, D.J. 2006 Laboratory generation of internal waves from sinusoidal topography. *Deep Sea Res. II: Topic. Stud. Oceanogr.* **53** (1-2), 96–115.

ALFORD, M.H., *et al*. 2011 Energy flux and dissipation in luzon strait: two tales of two ridges. *J. Phys. Oceanogr.* **41** (11), 2211–2222.

ALFORD, M.H., KLYMAK, J.M. & CARTER, G.S. 2014 Breaking internal Lee waves at Kaena Ridge, Hawaii. *Geophys. Res. Lett.* **41** (3), 906–912.

ALFORD, M.H., MACKINNON, J.A., ZHAO, Z., PINKEL, R., KLYMAK, J. & PEACOCK, T. 2007 Internal waves across the Pacific. *Geophys. Res. Lett.* **34**, L24601.

ALTHAUS, A.M., KUNZE, E. & SANFORD, T.B. 2003 Internal tide radiation from mendocino escarpment. *J. Phys. Oceanogr.* **33** (7), 1510–1527.

ARMENIO, V. & SARKAR, S. 2002 An investigation of stably stratified turbulent channel flow using large-eddy simulation. *J. Fluid Mech.* **459**, 1–42.

BAINES, P.G. & HOINKA, K.P. 1985 Stratified flow over two-dimensional topography in fluid of infinite depth: a laboratory simulation. *J. Atmos. Sci.* **42** (15), 1614–1630.

BALMFORTH, N.J., IERLEY, G.R. & YOUNG, W.R. 2002 Tidal conversion by subcritical topography. *J. Phys. Oceanogr.* **32** (10), 2900–2914.

BELL, T.H. 1975 Lee waves in stratified flows with simple harmonic time dependence. *J. Fluid Mech.* **67** (4), 705–722.

BUIJSMAN, M.C., LEGG, S. & KLYMAK, J. 2012 Double-ridge internal tide interference and its effect on dissipation in luzon strait. *J. Phys. Oceanogr.* **42** (8), 1337–1356.

CACCHIONE, D. & WUNSCH, C. 1974 Experimental study of internal waves over a slope. *J. Fluid Mech.* **66** (2), 223–239.

CARTER, G.S., GREGG, M.C. & LIEN, R.-C. 2005 Internal waves, solitary-like waves, and mixing on the monterey bay shelf. *Cont. Shelf Res.* **25** (12-13), 1499–1520.

CHALAMALLA, V.K. & SARKAR, S. 2015 Mixing, dissipation rate, and their overturn-based estimates in a near-bottom turbulent flow driven by internal tides. *J. Phys. Oceanogr.* **45** (8), 1969–1987.

CUSACK, J.M., VOET, G., ALFORD, M.H., GIRTON, J.B., CARTER, G.S., PRATT, L.J., Pearson-Potts, K.A. & Tan, S. 2019 Persistent turbulence in the samoan passage. *J. Phys. Oceanogr.* **49** (12), 3179–3197.

FRINGER, O.B. & STREET, R.L. 2003 The dynamics of breaking progressive interfacial waves. *J. Fluid Mech.* **494**, 319–353.

GALPERIN, B., KANTHA, L.H., MELLOR, G.L. & ROSATI, A. 1989 Modeling rotating stratified turbulent flows with application to oceanic mixed layers. *J. Phys. Oceanogr.* **19** (7), 901–916.

GARRETT, C. & KUNZE, E. 2007 Internal tide generation in the deep ocean. *Annu. Rev. Fluid Mech.* **39**, 57–87.

GAYEN, B. & SARKAR, S. 2010 Turbulence during the generation of internal tide on a critical slope. *Phys. Rev. Lett.* **104** (21), 218502.

GAYEN, B. & SARKAR, S. 2011 Direct and large-eddy simulations of internal tide generation at a near-critical slope. *J. Fluid Mech.* **681**, 48–79.

GEMMRICH, J. & KLYMAK, J.M. 2015 Dissipation of internal wave energy generated on a critical slope. *J. Phys. Oceanogr.* **45** (9), 2221–2238.

GIRTON, J.B., *et al*. 2019 Flow-topography interactions in the samoan passage. *Oceanography* **32** (4), 184–193.

HALL, R.A., HUTHNANCE, J.M. & WILLIAMS, R.G. 2013 Internal wave reflection on shelf slopes with depth-varying stratification. *J. Phys. Oceanogr.* **43** (2), 248–258.

HOLLOWAY, P.E. & MERRIFIELD, M.A. 1999 Internal tide generation by seamounts, ridges, and islands. *J. Geophys. Res.: Oceans* **104** (C11), 25937–25951.

HULT, E.L., TROY, C.D. & KOSEFF, J.R. 2006 Laboratory images of breaking internal waves. *Phys. Fluids* **18** (9), 091107.

IVEY, G.N. & NOKES, R.I. 1989 Vertical mixing due to the breaking of critical internal waves on sloping boundaries. *J. Fluid Mech.* **204**, 479–500.

IVEY, G.N., WINTERS, K.B. & DE SILVA, I.P.D. 2000 Turbulent mixing in a sloping benthic boundary layer energized by internal waves. *J. Fluid Mech.* **418**, 59–76.

JALALI, M., RAPAKA, N.R. & SARKAR, S. 2014 Tidal flow over topography: effect of excursion number on wave energetics and turbulence. *J. Fluid Mech.* **750**, 259–283.

JALALI, M. & SARKAR, S. 2017 Large eddy simulation of flow and turbulence at the steep topography of luzon strait. *Geophys. Res. Lett.* **44** (18), 9440–9448.

JAVAM, A., IMBERGER, J. & ARMFIELD, S.W. 1999 Numerical study of internal wave reflection from sloping boundaries. *J. Fluid Mech.* **396**, 183–201.

KANG, D. & FRINGER, O. 2010 On the calculation of available potential energy in internal wave fields. *J. Phys. Oceanogr.* **40** (11), 2539–2545.

KANG, D. & FRINGER, O. 2012 Energetics of barotropic and baroclinic tides in the Monterey Bay area. *J. Phys. Oceanogr.* **42** (2), 272–290.

KANTHA, L.H., ROSATI, A. & GALPERIN, B. 1989 Effect of rotation on vertical mixing and associated turbulence in stratified fluids. *J. Geophys. Res.: Oceans* **94** (C4), 4843–4854.

KHATIWALA, S. 2003 Generation of internal tides in an ocean of finite depth: analytical and numerical calculations. *Deep Sea Res. I: Oceanogr. Res. Papers* **50** (1), 3–21.

KLEMA, M., VENAYAGAMOORTHY, S.K., POUQUET, A., ROSENBERG, D. & MARINO, R. 2023 Effect of rotation on mixing efficiency in homogeneous stratified turbulence using unforced direct numerical simulations. *Environ. Fluid Mech.* **23**, 1115–1130.

KLYMAK, J.M., BUIJSMAN, M., LEGG, S. & PINKEL, R. 2013 Parameterizing surface and internal tide scattering and breaking on supercritical topography: the one-and two-ridge cases. *J. Phys. Oceanogr.* **43** (7), 1380–1397.

KLYMAK, J.M., LEGG, S., ALFORD, M.H., BUIJSMAN, M., PINKEL, R. & NASH, J.D. 2012 The direct breaking of internal waves at steep topography. *Oceanography* **25** (2), 150–159.

KLYMAK, J.M., LEGG, S. & PINKEL, R. 2010 A simple parameterization of turbulent tidal mixing near supercritical topography. *J. Phys. Oceanogr.* **40** (9), 2059–2074.

KLYMAK, J.M., MOUM, J.N., NASH, J.D., KUNZE, E., GIRTON, J.B., CARTER, G.S., LEE, C.M., SANFORD, T.B. & GREGG, M.C. 2006 An estimate of tidal energy lost to turbulence at the Hawaiian ridge. *J. Phys. Oceanogr.* **36** (6), 1148–1164.

KUNDU, P.K., COHEN, I.M. & DOWLING, D.W. 2008 *Fluid Mechanics*, 4th edn. Elsevier.

KUNZE, E. & SMITH, S.G L. 2004 The role of small-scale topography in turbulent mixing of the global ocean. *Oceanography* **17** (1), 55–64.

LAMB, K.G. 2014 Internal wave breaking and dissipation mechanisms on the continental slope/shelf. *Annu. Rev. Fluid Mech.* **46**, 231–254.

LAMB, K.G. & DUNPHY, M. 2018 Internal wave generation by tidal flow over a two-dimensional ridge: energy flux asymmetries induced by a steady surface trapped current. *J. Fluid Mech.* **836**, 192–221.

LAURENT, L.S., STRINGER, S., GARRETT, C. & PERRAULT-JONCAS, D. 2003 The generation of internal tides at abrupt topography. *Deep Sea Res. I: Oceanogr. Res. Papers* **50** (8), 987–1003.

LEDWELL, J.R., ST. LAURENT, L.C., GIRTON, J.B. & TOOLE, J.M. 2011 Diapycnal mixing in the antarctic circumpolar current. *J. Phys. Oceanogr.* **41** (1), 241–246.

LEGG, S. 2014 Scattering of low-mode internal waves at finite isolated topography. *J. Phys. Oceanogr.* **44** (1), 359–383.

LEGG, S. & ADCROFT, A. 2003 Internal wave breaking at concave and convex continental slopes. *J. Phys. Oceanogr.* **33** (11), 2224–2246.

LEGG, S. & KLYMAK, J. 2008 Internal hydraulic jumps and overturning generated by tidal flow over a tall steep ridge. *J. Phys. Oceanogr.* **38** (9), 1949–1964.

LEVINE, M.D. & BOYD, T.J. 2006 Tidally forced internal waves and overturns observed on a slope: results from home. *J. Phys. Oceanogr.* **36** (6), 1184–1201.

LINDBORG, E. 2005 The effect of rotation on the mesoscale energy cascade in the free atmosphere. *Geophys. Res. Lett.* **32**, 1–4.

LLEWELLYN SMITH, S.G. & YOUNG, W.R. 2002 Conversion of the barotropic tide. *J. Phys. Oceanogr.* **32** (5), 1554–1566.

LLEWELLYN SMITH, S.G. & YOUNG, W.R. 2003 Tidal conversion at a very steep ridge. *J. Fluid Mech.* **495**, 175–191.

MOORE, C.D., KOSEFF, J.R. & HULT, E.L. 2016 Characteristics of bolus formation and propagation from breaking internal waves on shelf slopes. *J. Fluid Mech.* **791**, 260–283.

MUNK, W. & WUNSCH, C. 1998 Abyssal recipes II: energetics of tidal and wind mixing. *Deep Sea Res. I: Oceanogr. Res. Papers* **45** (12), 1977–2010.

MUSGRAVE, R.C., MACKINNON, J.A., PINKEL, R., WATERHOUSE, A.F., NASH, J. & KELLY, S.M. 2017 The influence of subinertial internal tides on near-topographic turbulence at the mendocino ridge: observations and modeling. *J. Phys. Oceanogr.* **47** (8), 2139–2154.

MUSGRAVE, R.C., PINKEL, R., MACKINNON, J.A., MAZLOFF, M.R. & YOUNG, W.R. 2016 Stratified tidal flow over a tall ridge above and below the turning latitude. *J. Fluid Mech.* **793**, 933–957.

NASH, J.D., KUNZE, E., TOOLE, J.M. & SCHMITT, R.W. 2004 Internal tide reflection and turbulent mixing on the continental slope. *J. Phys. Oceanogr.* **34** (5), 1117–1134.

NIKURASHIN, M. & LEGG, S. 2011 A mechanism for local dissipation of internal tides generated at rough topography. *J. Phys. Oceanogr.* **41** (2), 378–395.

ORLANSKI, I. 1976 A simple boundary condition for unbounded hyperbolic flows. *J. Comput. Phys.* **21** (3), 251–269.

PERFECT, B., KUMAR, N. & RILEY, J.J. 2020*a* Energetics of seamount wakes. Part I: energy exchange. *J. Phys. Oceanogr.* **50** (5), 1365–1382.

PERFECT, B., KUMAR, N. & RILEY, J.J. 2020*b* Energetics of seamount wakes. Part II: wave fluxes. *J. Phys. Oceanogr.* **50** (5), 1383–1398.

PHILLIPS, O.M. 1977 *The Dynamics of the Upper Ocean*. Cambridge University Press.

PINKEL, R., BUIJSMAN, M. & KLYMAK, J.M. 2012 Breaking topographic lee waves in a tidal channel in luzon strait. *Oceanography* **25** (2), 160–165.

POLZIN, K.L. 2009 An abyssal recipe. *Ocean Model.* **30** (4), 298–309.

PUTHAN, P., JALALI, M., ORTIZ-TARIN, J.L., CHONGSIRIPINYO, K., PAWLAK, G. & SARKAR, S. 2020 The wake of a three-dimensional underwater obstacle: effect of bottom boundary conditions. *Ocean Model.* **149**, 101611.

PUTHAN, P., PAWLAK, G. & SARKAR, S. 2022 Wake vortices and dissipation in a tidally modulated flow past a three-dimensional topography. *J. Geophys. Res.: Oceans* **127** (8), e2022JC018470.

PUTHAN, P., SARKAR, S. & PAWLAK, G. 2021 Tidal synchronization of lee vortices in geophysical wakes. *Geophys. Res. Lett.* **48** (4), e2020GL090905.

RAPAKA, N.R., GAYEN, B. & SARKAR, S. 2013 Tidal conversion and turbulence at a model ridge: direct and large eddy simulations. *J. Fluid Mech.* **715**, 181–209.

RAY, R.D. & MITCHUM, G.T. 1996 Surface manifestation of internal tides generated near hawaii. *Geophys. Res. Lett.* **23** (16), 2101–2104.

SARKAR, S. & SCOTTI, A. 2017 From topographic internal gravity waves to turbulence. *Annu. Rev. Fluid Mech.* **49**, 195–220.

SHAKESPEARE, C.J. & HOGG, A.M. 2019 On the momentum flux of internal tides. *J. Phys. Oceanogr.* **49** (4), 993–1013.

SLINN, D.N. & RILEY, J.J. 1998 A model for the simulation of turbulent boundary layers in an incompressible stratified flow. *J. Comput. Phys.* **144** (2), 550–602.

SRINIVASAN, K., MCWILLIAMS, J.C., MOLEMAKER, M.J. & BARKAN, R. 2019 Submesoscale vortical wakes in the lee of topography. *J. Phys. Oceanogr.* **49** (7), 1949–1971.

ST. LAURENT, L. & GARRETT, C. 2002 The role of internal tides in mixing the deep ocean. *J. Phys. Oceanogr.* **32** (10), 2882–2899.

TROY, C.D. & KOSEFF, J.R. 2005 The instability and breaking of long internal waves. *J. Fluid Mech.* **543**, 107–136.

VENAYAGAMOORTHY, S.K. & FRINGER, O.B. 2005 Nonhydrostatic and nonlinear contributions to the energy flux budget in nonlinear internal waves. *Geophys. Res. Lett.* **32**, L15603.

VENAYAGAMOORTHY, S.K. & FRINGER, O.B. 2006 Numerical simulations of the interaction of internal waves with a shelf break. *Phys. Fluids* **18** (7), 076603.

VENAYAGAMOORTHY, S.K. & FRINGER, O.B. 2007 On the formation and propagation of nonlinear internal boluses across a shelf break. *J. Fluid Mech.* **577**, 137–159.

VLASENKO, V. & HUTTER, K. 2002 Numerical experiments on the breaking of solitary internal wavesover a slope–shelf topography. *J. Phys. Oceanogr.* **32** (6), 1779–1793.

WINTERS, K.B. & ARMI, L. 2013 The response of a continuously stratified fluid to an oscillating flow past an obstacle. *J. Fluid Mech.* **727**, 83–118.

WUNSCH, C. & FERRARI, R. 2004 Vertical mixing, energy, and the general circulation of the oceans. *Annu. Rev. Fluid Mech.* **36**, 281–314.

ZHENG, K. & NIKURASHIN, M. 2019 Downstream propagation and remote dissipation of internal waves in the Southern Ocean. *J. Phys. Oceanogr.* **49** (7), 1873–1887.